nature materials

Article

https://doi.org/10.1038/s41563-026-02537-2

Room-temperature two-dimensional multiferroic metal with voltage-controllable magnetic order

Received: 3 June 2025

Accepted: 10 February 2026

Published online: 09 March 2026

Check for updates

Dacheng Tian[1,3,11], Shulin Zhong[2,11], Jianyu Dong[1,3,11], Song Zhou[1,3], Zhiwen Liu[4], Kai Chen[5], Wenhua Zhang[5], Liang Cao[6], Xiaoyue He[7], Xiu Li[7], Tengyu Guo[7], Kunrong Du[8], Haifeng Feng[8], Yu Wang[1], Peng Cheng[1,3], Yiqi Zhang[1,3], Baojie Feng[1,3], Kehui Wu[9], Suhuai Wei[10], Yi Du[8] ✉, Yunhao Lu[2] ✉ & Lan Chen[1,3] ✉

Realizing two-dimensional multiferroics with robust magnetoelectric coupling for electric-field-controlled magnetism at room temperature poses substantial challenges, as ferroelectricity and magnetism inherently conflict. Here we report air-stable bilayer $CrTe_2$ that exhibits intrinsic room-temperature multiferroicity. Structural and magnetic characterization reveals an alternating ferromagnetic and antiferromagnetic bilayer architecture, driven by interlayer charge transfer that spontaneously breaks inversion symmetry and generates a switchable out-of-plane ferroelectric polarization. Scanning probe microscopy confirms the non-volatile control of magnetization states with an electric field, enabling electrical writing and magnetic reading functionalities. This mechanism, rooted in interlayer charge transfer, rather than conventional spin-orbit coupling, provides a foundation for engineering multiferroics with layered systems. The demonstration of a two-dimensional multiferroic material with magnetoelectric coupling under ambient conditions provides opportunities for energy-efficient memory devices and quantum sensing technologies.

Multiferroic materials[1–7], which integrate ferroelectric and magnetic orders through magnetoelectric (ME) coupling[2–5], enable the control of magnetism with an electric field—a capability for ultralow-power spintronic memory and quantum technologies. However, bulk multiferroics such as $BiFeO_3$ (ref. 6) and $TbMnO_3$ (ref. 7) face enduring limitations: small polarization magnitudes, weak ME coefficients (<100 V cm^{-1} Oe^{-1}), and ambient instability due to oxygen vacancy-induced leakage currents[8–10], collectively restricting their practical utility.

The rise of two-dimensional (2D) materials[11–13] has provided opportunities to circumvent these challenges via atomic-scale engineering. Yet, despite strategies such as quantum confinement and interfacial design[14–16], room-temperature 2D multiferroics with robust ME coupling remain unrealized[3–5]. Proposed intrinsic systems, such as NiI_2 (refs. 17–19) (where helical magnetic order drives ferroelectricity), suffer from low magnetic transition temperatures (~21 K), air sensitivity and unverified ME coupling. Similarly, artificial

[1]Institute of Physics, Chinese Academy of Sciences, Beijing, China. [2]School of Physics, State Key Laboratory of Silicon Materials and Advanced Semiconductor Materials, Zhejiang University, Hangzhou, China. [3]School of Physical Sciences, University of Chinese Academy of Sciences, Beijing, China. [4]Oxford Instruments Technology China, Beijing, China. [5]National Synchrotron Radiation Laboratory, University of Science and Technology of China, Hefei, China. [6]Anhui Key Laboratory of Low Energy Quantum Materials and Devices, High Magnetic Field Laboratory, HFIPS, Chinese Academy of Sciences, Hefei, China. [7]Songshan Lake Materials Laboratory, Dongguan, China. [8]School of Physics, Beihang University, Beijing, China. [9]Tsientang Institute for Advanced Study, Zhejiang, China. [10]Eastern Institute of Technology, Ningbo, China. [11]These authors contributed equally: Dacheng Tian, Shulin Zhong, Jianyu Dong. ✉e-mail: yi_du@buaa.edu.cn; luyh@zju.edu.cn; lchen@iphy.ac.cn

https://doi.org/10.1038/s41563-026-02537-2

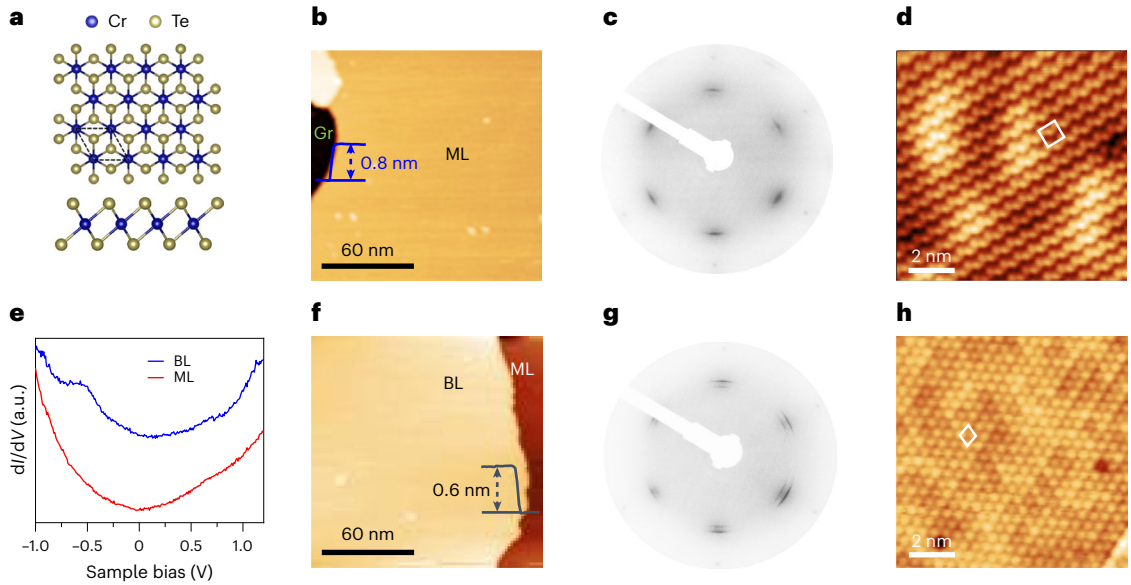

Fig. 1 | Atomic-scale structural and electronic characterization of monolayer and bilayer $CrTe_2$. **a**, Top view (upper) and side view (lower) of the lattice structure of 1T-$CrTe_2$, where Cr atoms (blue spheres) are sandwiched by Te atoms (yellow spheres), forming a vdW layered structure. **b**, STM topographic image of epitaxial monolayer $CrTe_2$ on a graphene/SiC(0001) substrate (scanning parameters: sample bias voltage (V_s) = −0.5 V, tunnelling current (I) = 50 pA). The line profile across the step of $CrTe_2$ with respect to graphene (Gr) shows the monolayer thickness. ML, monolayer. **c**, LEED pattern of monolayer $CrTe_2$ on graphene/SiC(0001) (electron energy: 90 eV), confirming a single hexagonal lattice with a lattice constant of 0.37 nm. **d**, High-resolution SP-STM image obtained using a Cr-coated tip (V_s = −0.1 V, I = 200 pA) on the surface of monolayer $CrTe_2$, revealing a zigzag-like pattern. White rectangle indicates unit cell. **e**, Differential conductance (dI/dV) spectra, showing the change in tunnelling current (I) with respect to the change in bias voltage (V), for monolayer (red) and bilayer (blue) $CrTe_2$, demonstrating metallic behaviour. BL, bilayer. **f**, STM topographic image of bilayer $CrTe_2$ (V_s = −0.5 V, I = 50 pA). The line profile across the step of the second layer of $CrTe_2$ with respect to the first layer shows the monolayer thickness. **g**, LEED pattern of bilayer $CrTe_2$ (electron energy: 90 eV) reveals two types of hexagonal lattice with constants of 0.37 nm (outer spots) and 0.39 nm (inner spots). **h**, High-resolution SP-STM image (V_s = −0.1 V, I = 200 pA) on the surface of bilayer $CrTe_2$ shows a hexagonal lattice constant of 0.39 nm. White rhombus indicates unit cell.

heterostructures[15,16]—stacking 2D ferroelectrics[20,21] and van der Waals (vdW) magnets[22–24]—are plagued by weak interfacial interactions, structural fragility and an inefficient ME response. Thus, the realization of air-stable 2D multiferroics with strong ME coupling at room temperature persists as a critical unresolved challenge, and demands innovative design models to overcome material limitations[1,3,25].

In this Article we address this gap with bilayer chromium telluride ($CrTe_2$), a room-temperature-stable 2D multiferroic synthesized via molecular beam epitaxy (MBE). This system demonstrates robust ferromagnetism, switchable out-of-plane (OOP) ferroelectricity and strong ME coupling under ambient conditions. Scanning tunnelling microscopy (STM) and low-energy electron diffraction (LEED) reveal an alternating antiferromagnetic/ferromagnetic (AFM/FM) layered structure, where interlayer electrostatic potential differences break symmetry to generate reversible polarization. Crucially, the ME coupling mechanism arises from electron filling in 2D metallic layers—a paradigm that is distinct from conventional spin-orbit coupling (SOC)—enabling the direct modulation of magnetic ordering and exchange interactions. This electron-filling-driven approach establishes a novel design principle for achieving strong ME effects in vdW systems, circumventing traditional limitations. Bilayer $CrTe_2$ not only surmounts long-standing material barriers but also pioneers the electric field manipulation of magnetism, unlocking pathways towards voltage-controlled quantum devices and energy-efficient spintronics.

Van der Waals epitaxial growth of $CrTe_2$

$CrTe_2$ crystallizes in a trigonal layered structure (space group $P\bar{3}m1$), where each layer adopts a 1T-type configuration. In this structure (Fig. 1a), Cr cations occupy the centres of Te octahedra, forming a covalently bonded in-plane (IP) network with interlayer vdW interactions. In our experiments, the uniform monolayer and bilayer $CrTe_2$ films were epitaxially grown on graphene/SiC(0001) substrates through MBE by optimizing the Cr/Te flux ratio and substrate temperature during growth. The samples were then transferred to another ultrahigh-vacuum (UHV) chamber for the in situ characterization.

Figure 1b shows a typical STM topographic image of as-grown monolayer $CrTe_2$ on a graphene/SiC(0001) substrate, with a layer thickness of 0.8 nm relative to the substrate. The LEED patterns of this sample (Fig. 1c) show six obvious spots, corresponding to the lattice constant of 0.37 nm for monolayer $CrTe_2$. A high-resolution STM image of monolayer $CrTe_2$ obtained at −0.1 V (Fig. 1d) via the adsorption of excess Cr adatoms at the tip apex, resolves a clear zigzag-like pattern with a unit cell of a = 0.74 nm, b = 0.64 nm. This feature refers to a $2 \times \sqrt{3}$ reconstruction with respect to the lattice constant of 0.37 nm, consistent with the zigzag-antiferromagnetic (z-AFM) order in monolayer $CrTe_2$ on the graphene/SiC(0001) substrate, as observed using spin-polarized STM (SP-STM) in previous work[26–29].

Figure 1f presents a typical STM topographic image of nearly bilayer $CrTe_2$ on a graphene/SiC(0001) substrate. The second layer of $CrTe_2$ exhibits an apparent layer thickness of 0.6 nm relative the first layer, consistent with previous experimental[26–28] and theoretical results. The LEED patterns of this sample (Fig. 1g) show two sets of spots that correspond to two kinds of lattice constant: 0.37 nm (outer) and 0.39 nm (inner). A high-resolution SP-STM image (Fig. 1h) shows that the surface of second-layer $CrTe_2$ exhibits a hexagonal close-packed arrangement with a lattice constant of $a = b$ = 0.39 nm, corresponding to the inner spots in the LEED pattern shown in Fig. 1g, whereas the outer spots should originate from the first layer of $CrTe_2$. According to the earlier work of Miao et al. in ref. 26, the hexagonal close-packed arrangements indicate that the second layer of $CrTe_2$ is FM. On the basis of the SP-STM and LEED measurements, it is possible that the first and second layers of $CrTe_2$ exhibit different magnetic orders. The dI/dV curves for monolayer and bilayer $CrTe_2$ (Fig. 1e) demonstrate the metallic behaviour in both samples. In addition, monolayer and bilayer

https://doi.org/10.1038/s41563-026-02537-2

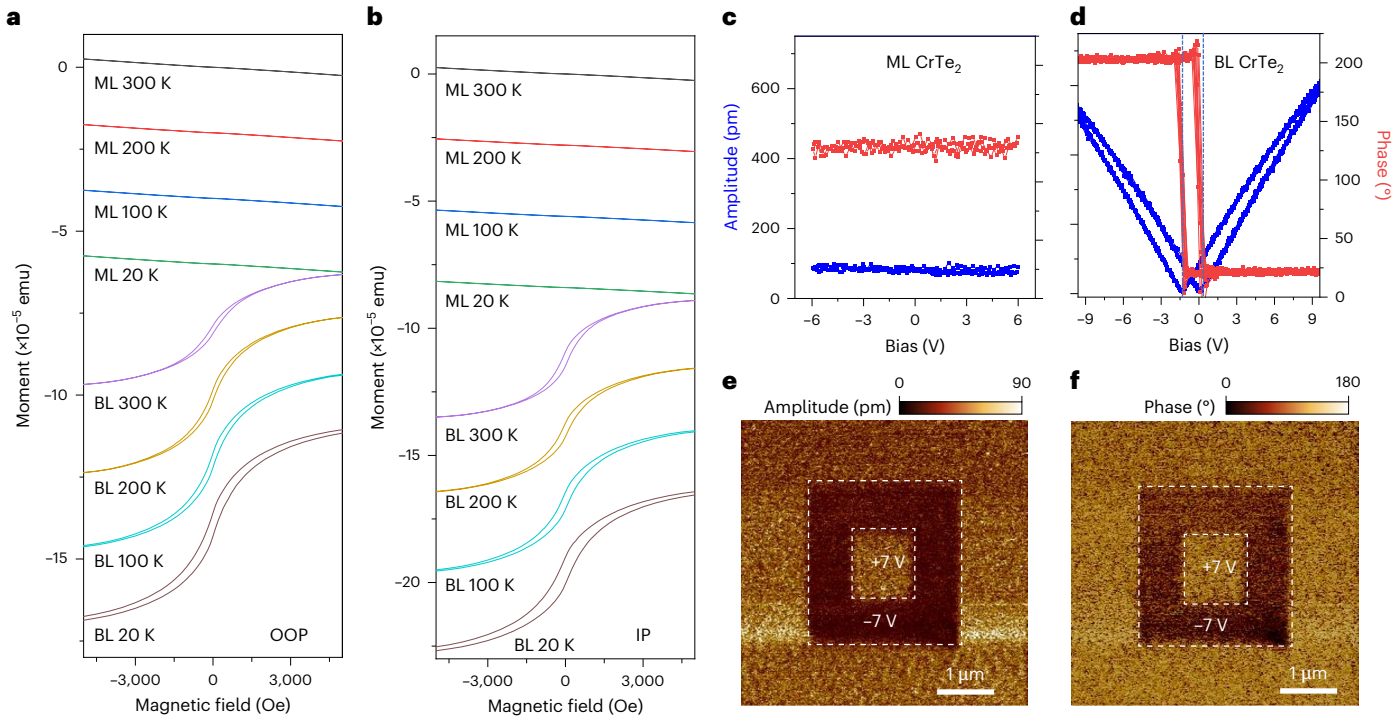

Fig. 2 | Room-temperature multiferroicity of bilayer $CrTe_2$. **a**,**b**, OOP (**a**) and IP (**b**) temperature-dependent magnetic hysteresis loops via SQUID measurements for monolayer and bilayer $CrTe_2$ on graphene/SiC(0001). **c**,**d**, PFM phase and amplitude loops for monolayer $CrTe_2$ (**c**) and bilayer $CrTe_2$ (**d**) measured at room temperature and in air. The ferroelectric hysteresis loop only exists in bilayer $CrTe_2$ **e**,**f**, OOP PFM amplitude (**e**) and phase (**f**) images after a box-in-box pattern with opposite DC bias (+7 and −7 V) writing is performed.

$CrTe_2$ on graphene/SiC(0001) substrates are stable under ambient conditions. After the sample was exposed to ambient conditions for two weeks, the two main characteristic vibration modes of E_{2g} and A_{1g}, located at 126.6 and 142.9 cm^{-1}, respectively, were still observed in the Raman spectra (Supplementary Fig. 1a), which is in good agreement with bulk $CrTe_2$ (Supplementary Fig. 1b) and previous studies[30,31].

Ferromagnetic and ferroelectric order in bilayer $CrTe_2$

The high quality and ambient stability of monolayer and bilayer $CrTe_2$ films on graphene/SiC(0001) substrates enable exploration of their magnetic ground states via macroscopic magnetic characterization using a superconducting quantum interference device (SQUID). After sample preparation and characterization in UHV chambers, the samples were taken out and exposed to air for the SQUID measurements. The magnetic properties of the monolayer and bilayer $CrTe_2$ thin films were examined in both OOP and IP configurations, as shown in Fig. 2a,b, respectively. For monolayer $CrTe_2$, both the OOP and IP magnetization–magnetic field strength (M–H) hysteresis loops at various temperatures (20–300 K) show paramagnetic signals from the substrate in the low magnetic field range (from −4,500 to 4,500 Oe). This behaviour is consistent with the z-AFM pattern observed in the SP-STM image (Fig. 1d) and aligns with previous studies[26–28]. Besides, the X-ray magnetic linear dichroism (XMLD) signal originates from anisotropic 3d–2p transition probabilities of Cr^{2+}/Cr^{3+} ions in an antiferromagnetically ordered environment, where opposite spin sublattices produce distinct linear-polarization-dependent absorption. The temperature-dependent disappearance of this dichroism reflects the collapse of spin-orbital anisotropy and confirms the AFM–paramagnetic transition of the Cr sublattice (Supplementary Fig. 2).

By contrast, bilayer $CrTe_2$ exhibits well-defined hysteresis loops at temperatures up to 300 K for both OOP (Fig. 2a) and IP (Fig. 2b) configurations. The saturation magnetization corresponds to approximately 2.44 μ_B per Cr ion at 20 K, in reasonable agreement with the 3.2 μ_B per Cr ion predicted from density functional theory (DFT) calculations at 0 K. The slightly smaller experimental value probably arises from finite-temperature spin fluctuations that reduce the effective magnetic moment. This consistency between the measured and calculated values is consistent with the magnetism originating from the intrinsic Cr 3d states rather than other impurities. In addition, the temperature-dependent magnetization (M–T) curves of bilayer $CrTe_2$ under an OOP magnetic field of 1,000 Oe confirms its room-temperature FM behaviour, as shown in Supplementary Fig. 3. To further confirm the intrinsic and layer-dependent magnetism, we performed element-specific X-ray magnetic circular dichroism (XMCD) measurements at the Cr $L_{2,3}$ absorption edges. As shown in Supplementary Fig. 4, a clear XMCD signal is detected for the bilayer $CrTe_2$ film even at room temperature, whereas the monolayer sample exhibits no detectable dichroism. The absence of XMCD in the monolayer is consistent with its compensated z-AFM order, whereas the finite dichroic response in the bilayer reflects the emergence of a net FM moment due to interlayer FM/z-AFM stacking. These results unambiguously indicate the different magnetic orders in monolayer and bilayer $CrTe_2$. Combining these results with the SP-STM measurements (Fig. 1d,h), we conclude that the first layer is AFM whereas the second layer is FM. Furthermore, the different lattice constants of the first and second layers of $CrTe_2$ indicate that the different magnetic orders may arise from the strain in the lattice of $CrTe_2$.

To investigate the presence of room-temperature ferroelectric $CrTe_2$, we conducted a comprehensive set of piezoresponse force microscopy (PFM) measurements under ambient conditions. Typically, applying a small voltage to the atomic force microscope tip induces a uniform dipole moment orientation in ferroelectric materials under the influence of a vertical electric field[32]. We recorded the off-field phase and amplitude loops on monolayer and bilayer $CrTe_2$, as shown in Fig. 2c,d, respectively. For monolayer $CrTe_2$, no discernible

https://doi.org/10.1038/s41563-026-02537-2

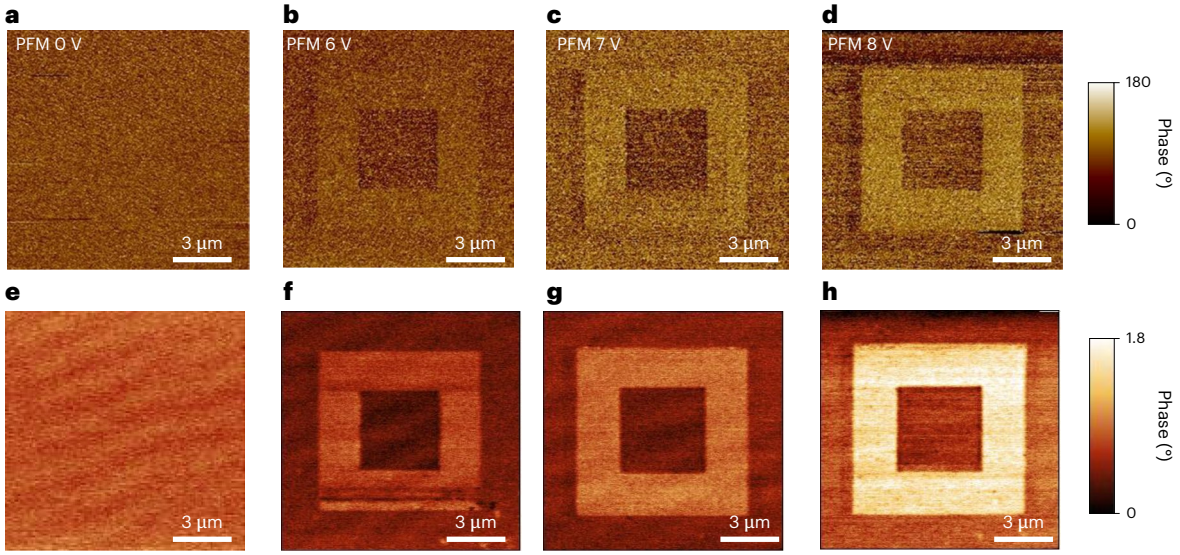

Fig. 3 | Electrical writing by PFM and magnetic reading by MFM for multiferroic bilayer $CrTe_2$. a–**d**, PFM images showing box-in-box ferroelectric domain structures for bilayer $CrTe_2$ on graphene/SiC(0001) written under applied voltages of 0 V (**a**), ±6 V (**b**), ±7 V (**c**) and ±8 V (**d**). **e**–**h**, MFM images of the same area on bilayer $CrTe_2$ taken after the PFM writing processes as in **a** (**e**), **b** (**f**), **c** (**g**) and **d** (**h**), showing magnetic domain reconfiguration after ferroelectric polarization writing. As the PFM writing bias is increased, the contrast with the opposite bias region of the written box becomes stronger, for both the PFM and MFM channels.

piezoresponse signal was detected (Fig. 2c), whereas a distinct hysteresis in the phase loop accompanied by a 180° phase switch and a well-defined butterfly-shaped amplitude evolution was observed on bilayer $CrTe_2$ (Fig. 2d). The local PFM switching spectra corroborate the OOP ferroelectricity that is inherent in bilayer $CrTe_2$. Furthermore, the coercive voltage was found to lie in the range of 1–2 V, which is comparable to that of intrinsic 2D ferroelectrics such as In_2Se_3 (1.5 V)[33] and SnS (2.0 V)[34].

Another hallmark of ferroelectric materials is domain engineering through an external electric field. We demonstrated polarization reversal in ferroelectric domains using PFM electrical 'read and write' operations. As shown in Fig. 2e,f, we wrote a distinct 'box in box' pattern with opposite direct-current (DC) bias (+7 and −7 V) on bilayer $CrTe_2$ and imaged the OOP amplitude and phase responses. Ultimately, on the basis of the SQUID, PFM and SP-STM measurements, we confirm the robust 2D multiferroic material in bilayer $CrTe_2$ under ambient conditions.

Electrical writing and magnetic reading for multiferroic bilayer $CrTe_2$

The effective ME coupling in multiferroic materials is crucial for their applications, as it enables the control of magnetic orders via an external electrical field. To verify the existence of ME coupling in bilayer $CrTe_2$ under ambient conditions, we conducted bias-dependent PFM and magnetic force microscopy (MFM) measurements on the same region of bilayer $CrTe_2$ on a graphene/SiC(0001) substrate. MFM operates by detecting the interactions between a magnetized conductive tip and the local magnetic field gradients emanating from the sample, providing topographic and magnetic interaction images over a specific region of sample at a fixed tip–sample separation. In our experiments, we carried out the electrical writing in PFM mode first, then conducted the magnetic reading in MFM mode.

A PFM phase image of the OOP response without domain writing was obtained on a clean and atomically flat region of bilayer $CrTe_2$ on a graphene/SiC(0001) substrate (Fig. 3a). Simultaneously, an MFM image taken in the same region reveals a normal fringe domain structure (Fig. 3e), indicating the FM nature of bilayer $CrTe_2$. Domain writing was then performed using a distinct box-in-box pattern by applying an opposite DC voltage bias (+6 and −6 V), as verified by the PFM amplitude image in Fig. 3b. Subsequent MFM measurement on the same region (Fig. 3f) shows two distinct magnetic domains with the same box-in-box pattern as the PFM electrical writing. The domain boundaries between the two domains with opposite writing voltage biases are clearly visible, demonstrating the robust ME coupling in bilayer $CrTe_2$. The ferroelectric domains created by electrical writing are recognizable as domains with different magnetic interactions, achieving the long-sought 'electrical writing and magnetic reading' functionality.

To rule out the contribution of electrostatic force, additional MFM measurements were performed using a non-magnetic conductive tip set to 0 V. The box-in-box writing pattern in PFM mode did not induce similar magnetic domains in MFM mode at various tip heights, as shown in Supplementary Fig. 5. Furthermore, as the applied opposite voltage biases in PFM mode were increased to +7 V (−7 V) and +8 V (−8 V), the amplitude contrast of the box-in-box patterm written by the opposite bias also increased (Fig. 3c,d). Simultaneously, the intensity contrast between the magnetic domains in MFM mode shows a similar trend (Fig. 3g,h), further confirming the existence of strong ME coupling in bilayer $CrTe_2$. Additional PFM and MFM measurements were carried out at a low bias (±1.5 V) and under a negative bias (−7 V). Negligible contrast is observed below ±2 V (Supplementary Fig. 6), defining the coercive threshold, whereas reversed PFM phase and MFM contrast appear under opposite writing polarities, confirming the reversible and bidirectional control of magnetism with an electric field (Supplementary Fig. 7).

In addition, it is noteworthy that such multiferroic properties and ME coupling are quite robust and stable, with the electrical writing and magnetic reading process remaining effective in the sample of bilayer $CrTe_2$ on graphene/SiC(0001) even after two weeks of exposure to ambient conditions (Supplementary Fig. 8). To assess the functional stability of the ferroic states, we monitored the evolution of the PFM and MFM contrasts of bilayer $CrTe_2$ under ambient exposure. As shown in Supplementary Fig. 9, both ferroelectric and magnetic contrasts decrease markedly within the first two weeks, retaining about 30% of their initial amplitude after 14 days. Beyond this point, the signals exhibit a pronounced saturation, with negligible additional attenuation up to 25 days. The persistent, correlated PFM and MFM responses

https://doi.org/10.1038/s41563-026-02537-2

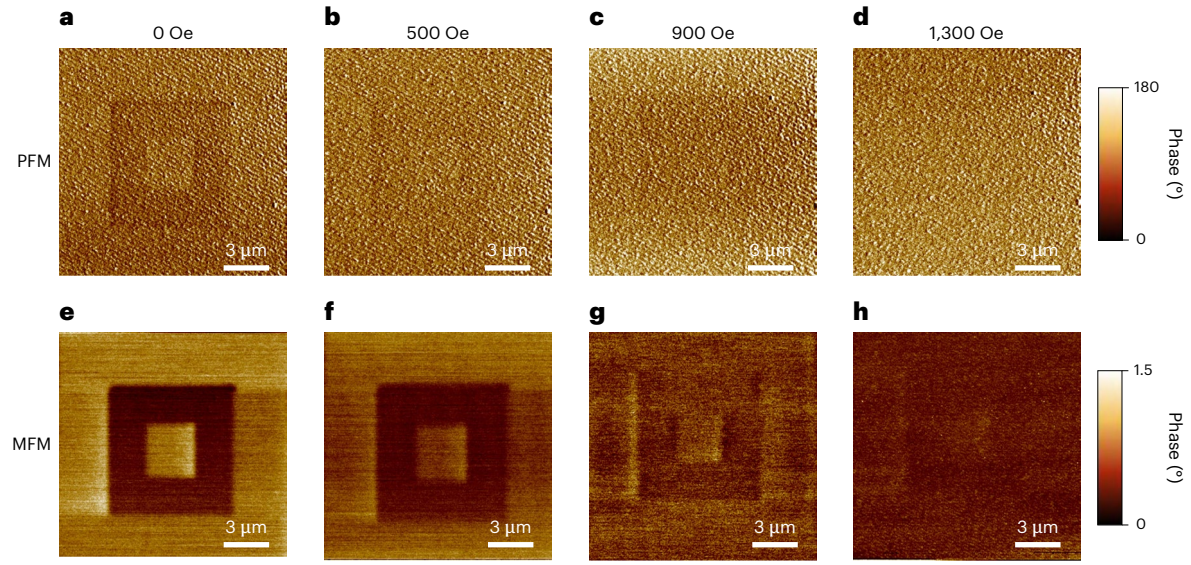

Fig. 4 | Magnetic-field-dependent PFM and MFM images of bilayer $CrTe_2$. **a**–**d**, PFM images showing box-in-box ferroelectric domain structures for bilayer $CrTe_2$ on graphene/SiC(0001) after writing under an applied magnetic field strength of 0 Oe (**a**), 500 Oe (**b**), 900 Oe (**c**) and 1,300 Oe (**d**). **e**–**h**, MFM images of the same area on bilayer $CrTe_2$ obtained under the corresponding magnetic field as in **a** (**e**), **b** (**f**), **c** (**g**) and **d** (**h**). Both ferroelectric (PFM) and magnetic (MFM) domain contrasts diminish progressively with increasing external magnetic field, reflecting magnetic-field-induced domain alignment and its influence on ferroelectric polarization through ME coupling.

confirm that the coupled ME order remains intact, despite partial attenuation of the measurable piezo- and magnetoresponses under ambient conditions.

To examine the evolution of the ferroic domains under external magnetic fields, we carried out sequential PFM and MFM imaging while gradually increasing the magnetic field strength. At zero field, the ferroelectric and magnetic domains exhibit sharp boundaries and strong contrast (Fig. 4a,e). As the magnetic field is increased, both the PFM and MFM contrasts progressively diminish, and the domain boundaries become increasingly indistinct (Fig. 4b,c,f,g). At field strength of 1,300 Oe (Fig. 4d,h), the images appear nearly uniform.

The origin of ferroelectricity

The bilayer $CrTe_2$ system, a 2D multiferroic material that exhibits robust ME coupling, displays distinct magnetic ordering in its monolayer and bilayer configurations, as demonstrated experimentally. This raises the possibility that ferroelectric order in bilayer $CrTe_2$ originates from magnetic order switching rather than conventional interlayer sliding mechanisms as proposed in previous studies[35–39]. To explain the origin of this ferroelectric behaviour, we developed a band model centred on magnetic-ordering-driven interlayer charge redistribution. The model posits that FM ordering stabilizes in electron-enriched layers, whereas AFM ordering becomes favourable in electron-depleted layers, driving spontaneous charge transfer between the layers. These predictions have been rigorously validated by first-principles DFT calculations, which strongly support the proposed interplay between magnetic and ferroelectric orders.

Monolayer $CrTe_2$ stabilizes both FM and z-AFM orders, exhibiting nearly degenerate total energies. As illustrated in Fig. 5a,b, the density of states (DOS) and band-filling characteristics of the Cr-t_{2g} and Cr-e_g orbitals are compared for FM and z-AFM configurations, respectively. In the FM state (Fig. 5a), the DOS exhibits pronounced spin-polarized splitting, with near-complete occupation of spin-up Cr-t_{2g} states and unoccupied spin-down states. Band-resolved calculations show that each Cr atom retains three valence electrons fully occupying the Cr-t_{2g} band, while excess electrons populate the Cr-e_g band. Although the hybridization between fully occupied Cr-t_{2g} orbitals does not lower total energy, the partial Cr-e_g occupancy (less than 25% filled) enables orbital hybridization between adjacent Cr sites. In the z-AFM configuration (Fig. 5b), Cr atoms with opposing spin orientations (↑ and ↓) exhibit equivalent *d*-orbital-filling characteristics. Both spin states exhibit partial occupation of the Cr-e_g orbitals and full occupation of the Cr-t_{2g} orbitals, whereas the antiparallel spin alignment between adjacent Cr atoms prevents direct e_g/t_{2g} orbital coupling. Similar to the case of the FM system, the fully occupied Cr-t_{2g} orbitals do not contribute to the total orbital energy of the z-AFM configuration. Hence, our analysis focuses primarily on the filling of the Cr-e_g bands. The coupling between fully filled Cr-e_g and partially filled Cr-e_g orbitals with parallel spin alignment leads to partial occupation of higher antibonding orbitals and fully occupied Cr-e_g orbitals, resulting in an energy-level difference between the Cr *d* orbitals of the monolayer FM and z-AFM systems.

In bilayer $CrTe_2$, the energy-level disparity between the two magnetic orders drives preferential electron transfer from the z-AFM to the FM configuration. Upon charge transfer, one layer prefers FM order because the increased electron occupancy in the Cr-e_g orbitals (approaching half-filling) strengthens Cr–Cr orbital hybridization, driving notable energetic stabilization of the system. The z-AFM order is stabilized in the other layer by the depletion of electrons from antibonding states. This depletion enhances the coupling between the fully occupied and empty Cr-e_g orbitals of adjacent Cr atoms that possess parallel spin alignment, thereby lowering the total energy of the z-AFM configuration. However, charge transfer from the z-AFM to the FM layer is also self-limited. When excessive electron transfer occurs, leading to over half-filling of the FM Cr-e_g band and non-full filling of the z-AFM Cr-e_g band (Fig. 5a,b), partially occupied antibonding (bonding) states that emerge from interactions between the e_g orbitals of the FM (z-AFM) order will destabilize the bilayer $CrTe_2$ and further charge transfer is prevented. This dual stabilization mechanism results in a direct relationship between the magnetic order stability and charge transfer (Fig. 5c). An energy minimum occurs at a charge transfer of approximately 0.019 C m^{-2}. Evidence for a magnetic order driving force for interlayer charge transfer is further shown by a ~0.1 eV electrostatic potential difference between z-AFM and FM monolayers (Fig. 5d), aligning with predictions from our band-filling model.

https://doi.org/10.1038/s41563-026-02537-2

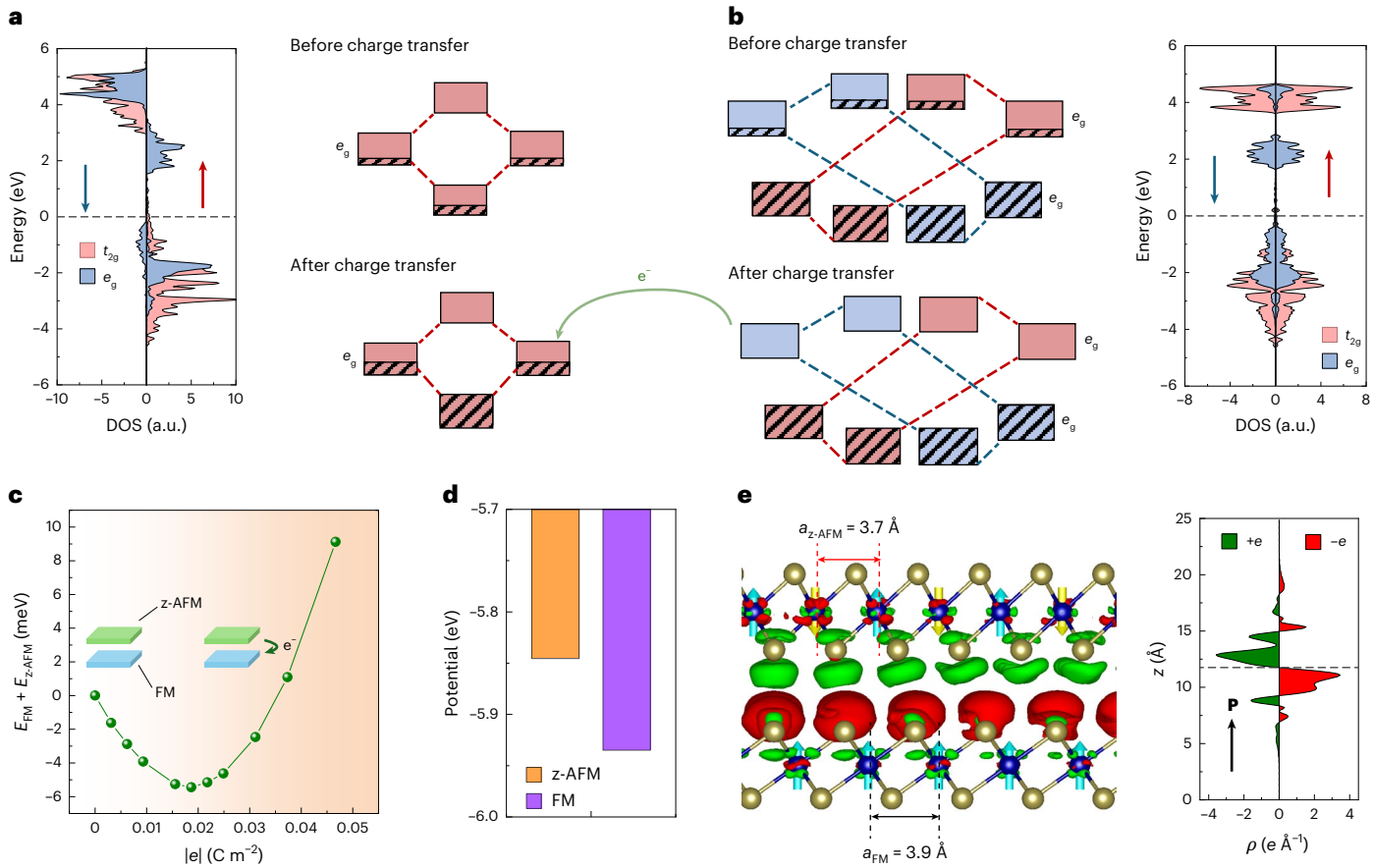

Fig. 5 | The occurrence the net polarization in metallic bilayer $CrTe_2$. **a**,**b**, DOS and band-filling characteristics of the Cr-t_{2g} and Cr-e_g orbitals for the FM configuration (**a**) and z-AFM configuration (**b**) of monolayer $CrTe_2$. Outermost plots: DOS diagrams for the Cr-t_{2g} and Cr-e_g orbitals. The region where DOS > 0 represents spin-up states (red arrow), and DOS < 0 represents spin-down states (blue arrow). Innermost diagrams: schematics of band filling (hatched pattern) and coupling (red dashed lines) between Cr-e_g orbitals before and after charge transfer. The red and blue shading denotes spin-up and spin-down bands, respectively. The green arrow indicates the electron-transfer direction. **c**, Total energy of the monolayer FM and z-AFM systems ($E_{FM} + E_{z\text{-}AFM}$) as a function of charge transfer via the magnitude of the surface charge density $|e|$, with hole accumulation for the z-AFM layer and electron accumulation for the FM layer. The energy of the undoped system is set to zero. The inset illustrates the corresponding structural schematic as the surface charge density increases, indicating charge transfer from the z-AFM to the FM configuration. The background colour shading indicates an increase of charge transfer. **d**, Electrostatic potential of monolayer $CrTe_2$ in the z-AFM and FM configurations, respectively. **e**, Left: differential charge density ($\Delta\rho = \rho_{z\text{-}AFM/FM} - \rho_{z\text{-}AFM} - \rho_{FM}$) of the z-AFM/FM bilayer superlattice. The red regions correspond to electron accumulation, whereas the green regions indicate areas of electron depletion. The spin orientations of each layer are indicated by blue (↑) and yellow (↓) arrows. The red dashed lines indicate the lattice constant for the z-AFM structure ($a_{z\text{-}AFM}$), and the black dashed lines delineate the lattice constant for the FM structure (a_{FM}). Right: the corresponding line profiles along the z direction for the z-AFM/FM bilayer superlattice. **P**, electric polarization field.

Differential charge density ($\Delta\rho$) analysis (Fig. 5e) directly corroborates this mechanism, revealing hole accumulation in the z-AFM layer and electron enrichment in the FM layer. A charge-transfer quantity of ~0.020 C m^{-2} is derived from our calculations (Fig. 5e, right panel). Notably, this value shows strong consistency with the energy minimum observed in Fig. 5c, and offers further evidence for the predicted charge redistribution process. This asymmetric charge redistribution generates a spontaneous polarization of ~3.0 pC m^{-1} along the z direction, surpassing the polarization strength of conventional sliding ferroelectric systems (0.1–1.2 pC m^{-1})[40–43]. Crucially, the polarization vector remains fixed across all interlayer sliding configurations (Supplementary Fig. 10), ruling out structural sliding as the origin of ferroelectricity. Remarkably, the charge-transfer process is reversible: switching the magnetic order of either layer (FM ↔ z-AFM) inverts the polarization direction, demonstrating a robust ME coupling.

Discussions

The origin of ferroelectricity in bilayer $CrTe_2$ from the switching of magnetic order in either $CrTe_2$ layer is also supported further by the experimental details in the PFM and STM measurements. For example, the hysteresis loop in Fig. 2d displays a pronounced asymmetry between positive and negative biases, reflected in unequal coercive fields and a finite loop shift. This behaviour demonstrates a built-in polarization arising from interfacial asymmetry and intrinsic charge transfer, which lowers the free energy of one ME domain configuration relative to its conjugate. The ensuing energetic bias governs the stability and sets different switching thresholds for opposite polarities, thereby shaping the dynamics of coupled ferroelectric and magnetic states. The +7 V biased region in Fig. 2e,f shows the same contrast as the unbiased region. This behaviour is consistent with a built-in polarization that already stabilizes the z-AFM(bottom)/FM(top) configuration. First-principles calculations under a positive OOP field reproduce this trend: the top layer gains charge while the bottom layer loses charge, which energetically favours z-AFM(bottom)/FM(top) over the reversed sequence. Moreover, SP-STM imaging shows the coexistence of two distinct magnetic–ferroelectric domain configurations in bilayer $CrTe_2$. In most regions, the magnetic contrast corresponds to the configuration with z-AFM order in the bottom layer and FM order

in the top layer, consistent with the ground-state stacking predicted by theory. Notably, in certain localized areas we also identify small domains that exhibit the reversed configuration, where z-AFM is in the top layer, as demonstrated by the opposite zigzag magnetic contrast and identical lattice registry (Supplementary Fig. 11a). The simultaneous observation of both domain types confirms the existence of two energetically competing yet nearly degenerate ME states, in excellent agreement with the theoretical model presented in Fig. 5, where switching the electric polarization interchanges the FM and z-AFM layers. These results provide direct microscopic evidence for polarization-dependent magnetic stacking, and demonstrate that the bilayer $CrTe_2$ system hosts coexisting dual ME states that are associated with opposite polarization orientations.

With the discovery of 2D magnetic materials, much effort has been devoted to achieving direct electrical control and manipulation of the magnetic properties in vdW materials exhibiting intrinsic type-II multiferroicity—a direct entanglement of magnetic and ferroelectric orders that arises from an inversion-symmetry-breaking spin configuration. Although type-II multiferroicity is a mechanism that inherently yields orders-of-magnitude stronger and more robust ME responses compared with conventional approaches, it relies highly on SOC that is difficult to survive against thermal fluctuation at room temperature. Our results emphasize the crucial role of electron filling of 2D metallic layers for modulating magnetic ordering and exchange interactions, instead of SOC. The electron filling ultimately determines the magnetic ground state of each layer between competing FM and AFM ordering, resulting in spontaneous charge transfer and polarization. Thus, an electric field enables non-volatile switching between FM and AFM orders in individual layers of bilayer $CrTe_2$ via interlayer charge transfer. This multiferroic mechanism, driven by two degenerate ground states with alternating FM/AFM layer stacking configurations, is exclusive to 2D vdW metallic $CrTe_2$, and emerges from a threefold design framework: (1) precise tuning of the conduction-band electron filling in the monolayer is critical, and requires an intermediate occupation regime that balances the electron filling between FM and AFM ordering to stabilize competing magnetic interactions; (2) as with a 2D ferroelectric metal, the system exhibits laterally conducting states that are confined to its 2D atomic layers while remaining vertically insulating, establishing an OOP ferroelectric polarization; and (3) the magnetic stabilization energy gained through the charge transfer between layers must outweigh the strain energy imposed by lattice mismatch between the FM and AFM layers to stabilize the coupled magnetic order, which is only possible in vdW layers. This complex magnetic ground state in an atomically thin vdW metallic crystal introduces a new approach by which to manipulate magnetic states via an electric field, using vdW engineering to tune the magnetic order through electron filling in 2D magnets. This approach facilitates the robust, direct electrical manipulation of magnetic states via external fields and reveals emergent interfacial multiferroic phenomena in engineered vdW heterostructures. Furthermore, gate-tunable ME coupling in 2D metallic systems provides a versatile platform for continuously directing multiferroic systems towards quantum critical regimes.

Conclusion

In this work we report a room-temperature and air-stable bilayer $CrTe_2$ multiferroic system that directly realizes electrical writing and magnetic reading functionality. Theoretical calculations, combined with STM, PFM and MFM measurements, confirm that the electrostatic potential difference between z-AFM and FM layers of $CrTe_2$ spontaneously breaks inversion symmetry, generating robust ferroelectric polarization. Distinct from conventional SOC-driven mechanisms in normal type-II multiferroic materials, this interlayer charge-asymmetry mechanism enables robust ME coupling, even at room temperature. The FM/AFM superlattice structure proposed here establishes a universal design principle for engineering 2D single-phase multiferroics. Notably, the room-temperature and air-stable electrical writing and magnetic reading demonstrated in bilayer $CrTe_2$ bridges the gap between fundamental multiferroic physics and scalable applications. This breakthrough positions 2D multiferroics as a viable platform for CMOS-compatible, energy-efficient spintronic memory, accelerating their integration into post-Moore nanoelectronics.

Online content

Any methods, additional references, Nature Portfolio reporting summaries, source data, extended data, supplementary information, acknowledgements, peer review information; details of author contributions and competing interests; and statements of data and code availability are available at https://doi.org/10.1038/s41563-026-02537-2.

References

1. Lu, C., Wu, M., Lin, L. & Liu, J.-M. Single-phase multiferroics: new materials, phenomena, and physics. *Natl Sci. Rev.* **6**, 653–668 (2019).
2. Schmid, H. Multi-ferroic magnetoelectrics. *Ferroelectrics* **162**, 317–338 (1994).
3. Fiebig, M., Lottermoser, T., Meier, D. & Trassin, M. The evolution of multiferroics. *Nat. Rev. Mater.* **1**, 16046 (2016).
4. Spaldin, N. A. & Ramesh, R. Advances in magnetoelectric multiferroics. *Nat. Mater.* **18**, 203–212 (2019).
5. Eerenstein, W., Mathur, N. D. & Scott, J. F. Multiferroic and magnetoelectric materials. *Nature* **442**, 759–765 (2006).
6. Wang, J. et al. Epitaxial $BiFeO_3$ multiferroic thin film heterostructures. *Science* **299**, 1719–1722 (2003).
7. Kimura, T. et al. Magnetic control of ferroelectric polarization. *Nature* **426**, 55–58 (2003).
8. Tomczyk, M., Mahajan, A., Tkach, A. & Vilarinho, P. M. Interface-based reduced coercivity and leakage currents of $BiFeO_3$ thin films: a comparative study. *Mater. Des.* **160**, 1322–1334 (2018).
9. Shin, H. W. & Son, J. Y. Leakage current characteristics of polycrystalline $BiFeO_3$ thin films affected by thickness-dependent domain wall currents. *J. Alloys Compd.* **968**, 172113 (2023).
10. Yang, H., Wang, Y. Q., Wang, H. & Jia, Q. X. Oxygen concentration and its effect on the leakage current in $BiFeO_3$ thin films. *Appl. Phys. Lett.* **96**, 012909 (2010).
11. Sun, Z. et al. Evidence for multiferroicity in single-layer $CuCrSe_2$. *Nat. Commun.* **15**, 4252 (2024).
12. Wang, X. et al. Electrical and magnetic anisotropies in van der Waals multiferroic $CuCrP_2S_6$. *Nat. Commun.* **14**, 840 (2023).
13. Hu, Q. et al. Ferrielectricity controlled widely-tunable magnetoelectric coupling in van der Waals multiferroics. *Nat. Commun.* **15**, 3029 (2024).
14. Molinari, A. et al. Hybrid supercapacitors for reversible control of magnetism. *Nat. Commun.* **8**, 15339 (2017).
15. Wang, Y. et al. Exploitable magnetic anisotropy and half-metallicity controls in multiferroic van der Waals heterostructure. *npj Comput. Mater.* **9**, 223 (2023).
16. Zhang, T. et al. Tunable Schottky barriers and magnetoelectric coupling driven by ferroelectric polarization reversal of MnI_3/In_2Se_3 multiferroic heterostructures. *npj Comput. Mater.* **10**, 238 (2024).
17. Amini, M. et al. Atomic-scale visualization of multiferroicity in monolayer NiI_2. *Adv. Mater.* **36**, 2311342 (2024).
18. Song, Q. et al. Evidence for a single-layer van der Waals multiferroic. *Nature* **602**, 601–605 (2022).
19. Gao, F. Y. et al. Giant chiral magnetoelectric oscillations in a van der Waals multiferroic. *Nature* **632**, 273–279 (2024).
20. Gou, J. et al. Two-dimensional ferroelectricity in a single-element bismuth monolayer. *Nature* **617**, 67–72 (2023).
21. Li, W. et al. Emergence of ferroelectricity in a nonferroelectric monolayer. *Nat. Commun.* **14**, 2757 (2023).

22. Gibertini, M., Koperski, M., Morpurgo, A. F. & Novoselov, K. S. Magnetic 2D materials and heterostructures. *Nat. Nanotechnol.* **14**, 408–419 (2019).
23. Mak, K. F., Shan, J. & Ralph, D. C. Probing and controlling magnetic states in 2D layered magnetic materials. *Nat. Rev. Phys.* **1**, 646–661 (2019).
24. Gong, C. & Zhang, X. Two-dimensional magnetic crystals and emergent heterostructure devices. *Science* **363**, eaav4450 (2019).
25. Ma, J., Hu, J., Li, Z. & Nan, C.-W. Recent progress in multiferroic magnetoelectric composites: from bulk to thin films. *Adv. Mater.* **23**, 1062–1087 (2011).
26. Miao, G. et al. Tuning the magnetism in ultrathin Cr_xTe_y films by lattice dimensionality. *Adv. Electron. Mater.* **11**, 2400720 (2024).
27. Xian, J.-J. et al. Spin mapping of intralayer antiferromagnetism and field-induced spin reorientation in monolayer $CrTe_2$. *Nat. Commun.* **13**, 257 (2022).
28. Yao, J. et al. Ultrathin van der Waals antiferromagnet $CrTe_3$ for fabrication of in-plane $CrTe_3$/$CrTe_2$ monolayer magnetic heterostructures. *Adv. Mater.* **34**, 2200236 (2022).
29. Li, R. et al. Planar heterojunction of ultrathin $CrTe_3$ and $CrTe_2$ van der Waals magnet. *ACS Nano* **16**, 4348–4356 (2022).
30. Meng, L. et al. Anomalous thickness dependence of Curie temperature in air-stable two-dimensional ferromagnetic 1T-$CrTe_2$ grown by chemical vapor deposition. *Nat. Commun.* **12**, 809 (2021).
31. Liu, J. et al. Si-CMOS cmpatible synthesis of wafer-scale 1T-$CrTe_2$ with step-like magnetic transition. *Adv. Mater.* **37**, 2414845 (2025).
32. Gruverman, A., Alexe, M. & Meier, D. Piezoresponse force microscopy and nanoferroic phenomena. *Nat. Commun.* **10**, 1661 (2019).
33. Zhou, Y. et al. Out-of-plane piezoelectricity and ferroelectricity in layered α-In_2Se_3 nanoflakes. *Nano Lett.* **17**, 5508–5513 (2017).
34. Bao, Y. et al. Gate-tunable in-plane ferroelectricity in few-layer SnS. *Nano Lett.* **19**, 5109–5117 (2019).
35. Li, L. & Wu, M. Binary compound bilayer and multilayer with vertical polarizations: two-dimensional ferroelectrics, multiferroics, and nanogenerators. *ACS Nano* **11**, 6382–6388 (2017).
36. Li, X. et al. Sliding ferroelectric memories and synapses based on rhombohedral-stacked bilayer MoS_2. *Nat. Commun.* **15**, 10921 (2024).
37. Sui, F. et al. Sliding ferroelectricity in van der Waals layered γ-InSe semiconductor. *Nat. Commun.* **14**, 36 (2023).
38. Meng, P. et al. Sliding induced multiple polarization states in two-dimensional ferroelectrics. *Nat. Commun.* **13**, 7696 (2022).
39. Chen, X., Ding, X., Gou, G. & Zeng, X. C. Strong sliding ferroelectricity and interlayer sliding controllable spintronic effect in two-dimensional HgI_2 layers. *Nano Lett.* **24**, 3089–3096 (2024).
40. Kim, S. K. et al. Directional dependent piezoelectric effect in CVD grown monolayer MoS_2 for flexible piezoelectric nanogenerators. *Nano Energy* **22**, 483–489 (2016).
41. Rogée, L. et al. Ferroelectricity in untwisted heterobilayers of transition metal dichalcogenides. *Science* **376**, 973–978 (2022).
42. Xue, F. et al. Multidirection piezoelectricity in mono- and multilayered hexagonal α-In_2Se_3. *ACS Nano* **12**, 4976–4983 (2018).
43. Esfahani, E. N., Li, T., Huang, B., Xu, X. & Li, J. Piezoelectricity of atomically thin WSe_2 via laterally excited scanning probe microscopy. *Nano Energy* **52**, 117–122 (2018).

Methods

Growth of $CrTe_2$/graphene/SiC(0001)

The $CrTe_2$ film was synthesized via MBE under UHV conditions (base vacuum 2×10^{-10} mbar). The graphene substrate was prepared by annealing a 4H-SiC(0001) substrate at 1,150 °C for 30 s and repeating this 100 times. After obtaining clear and atomically flat graphene, high-purity Cr and Te were evaporated from a tantalum boat and a standard Knudsen cell, with flux of 0.1 Å min^{-1} and 6 Å min^{-1}, respectively, with the temperature of the substrate kept at 350 °C. The structure of $CrTe_2$ was confirmed via LEED.

Scanning probe microscopy measurements

After sample preparation, it was transferred to the chamber of an STM instrument (Infinity STM, Ormicron) without breaking the vacuum. All STM images were acquired using a chemically etched tungsten tip at 10 K. The scanning tunnelling spectroscopy (STS) spectra were measured using lock-in technology with an alternating-current (AC) voltage of 20 mV and a superimposed frequency of 667 Hz on the bias voltage. The STM/STS data were acquired in constant-current mode. Atomic force microscopy, PFM and MFM measurements were carried out using a commercial scanning probe microscope (Asylum Research Cypher S, Oxford Instruments) at room temperature. PFM local switching spectroscopy was performed in dual AC resonance tracking (or DART) mode, with the superimposition of an AC signal over a series of DC triangular, sawtooth waveform voltages. The PFM phase and amplitude loops were recorded when the tip voltage was zero. The PFM and MFM measurements for ME coupling were performed using the same conductive magnetic tip (Co-Cr-doped); after writing a ferroelectric domain, the PFM image was first obtained and then the MFM image was measured. The PFM and MFM measurements under a magnetic field were carried out using a commercial scanning probe microscope (Asylum Research Jupiter Discovery, Oxford Instruments) equipped with a VFM4 component at room temperature.

Magnetic measurements

The magnetic measurements were carried out using a SQUID magnetometer (MPMS-3, Quantum Design). Soft X-ray absorption spectroscopy (XAS) and XMCD were conducted at the Hefei Light Source of the National Synchrotron Radiation Laboratory. The Cr $L_{2,3}$-edge XAS spectra were probed at beamlines MCD-A and MCD-B, and the signal of the total electron yield was measured at $T = 300$ K by switching the magnetic field parallel or antiparallel to the incoming X-ray beam. As a bend-magnet source, the circular (left/right) polarization of the X-rays was switched by adjusting the front aperture below or above the beam orbit. The right circular polarization of the beam, which was calibrated at ~65%, was fixed through the XMCD measurements. For each field (±0.35 T), four scans were recorded, and the XAS signals were processed using simple normalization as I/I_0, where I is the total electron yield signal of our sample and I_0 is the photocurrent from a gold mesh as a reference. This enabled us to recover the differences from the X-ray beam intensity (caused by the variation in the storage ring current due to the top-up injection mode) during each XAS measurement. The XMCD spectra were obtained by subtracting the averaged XAS spectrum detected under positive and negative magnetic fields. XMLD measurements were carried out at the same beamline under identical base pressure and photon-energy calibration conditions. The Cr $L_{2,3}$-edge XAS spectra were recorded in total electron yield mode using linearly polarized light. To extract the XMLD signal, two sets of XAS spectra were collected with the electric field vector of the incident X-rays oriented parallel ($\mathbf{E}_{\parallel}$) and perpendicular ($\mathbf{E}_{\perp}$) to the IP crystallographic axis of the sample, corresponding to normal and grazing incidence geometries, respectively. The XMLD intensity was obtained as the difference $\Delta I(E) = I(E_{\parallel}) - I(E_{\perp})$ after normalization to the edge jump. Temperature-dependent XMLD measurements were performed between 80 and 300 K to probe the evolution of the Cr 3*d* orbital anisotropy and magnetic ordering.

Raman spectroscopy

Raman spectroscopy was carried out using a LabRAM HR Evolution spectrometer with 532 nm laser excitation.

DFT calculations

The first-principles calculations are performed within the framework of DFT using the projector augmented-wave method[44,45] as implemented in the Vienna ab initio simulation package[46]. The exchange–correlation term is treated using the generalized-gradient approximation of the Perdew–Burke–Ernzerhof functional[47]. A plane-wave basis set with a kinetic energy cut-off of 500 eV was adopted for Kohn–Sham orbital expansion. The 2D Brillouin zone was sampled by a Monkhorst–Pack[48] k-point mesh, and it is 6 × 7 for all orthorhombic magnetic configurations. A sufficiently large vacuum layer of at least 20 Å along the OOP direction was adopted to eliminate the interaction among images. Dispersion correction was performed at the vdW-DF level[49], with the vdW-DF2 functional[50] for the exchange potential. The positions of the atoms were fully relaxed until the Hellmann–Feynman force on each atom was less than 0.005 eV $Å^{-1}$ and the energy difference between two consecutive self-consistent steps was less than 10^{-6} eV. To address strong electron correlation effects in Cr 3*d* orbitals, the DFT + U formalism[51,52] was applied with Hubbard parameters $U = 3.0$ eV and $J = 0.6$ eV, respectively. In the z-AFM/FM bilayer, FM–z-AFM lattice mismatch still held, and a precise superlattice comprising 1,356 atoms was implemented to constrain optimized lattice mismatch below 3%.

Data availability

Relevant data that support the key findings of this study are available within the Article and its Supplementary Information. All raw data generated during the current study are available from the corresponding authors upon request.

Code availability

The computer code used for numerical calculations and data processing is available from the corresponding authors upon request.

References

44. Blöchl, P. E. Projector augmented-wave method. *Phys. Rev. B* **50**, 17953–17979 (1994).
45. Kresse, G. & Joubert, D. From ultrasoft pseudopotentials to the projector augmented-wave method. *Phys. Rev. B* **59**, 1758–1775 (1999).
46. Kresse, G. & Furthmüller, J. Efficient iterative schemes for ab initio total-energy calculations using a plane-wave basis set. *Phys. Rev. B* **54**, 11169–11186 (1996).
47. Perdew, J. P., Burke, K. & Ernzerhof, M. Generalized gradient approximation made simple. *Phys. Rev. Lett.* **77**, 3865–3868 (1996).
48. Monkhorst, H. J. & Pack, J. D. Special points for Brillouin-zone integrations. *Phys. Rev. B* **13**, 5188–5192 (1976).
49. Dion, M., Rydberg, H., Schröder, E., Langreth, D. C. & Lundqvist, B. I. Van der Waals density functional for general geometries. *Phys. Rev. Lett.* **92**, 246401 (2004).
50. Lee, K., Murray, É. D., Kong, L., Lundqvist, B. I. & Langreth, D. C. Higher-accuracy van der Waals density functional. *Phys. Rev. B* **82**, 081101(R) (2010).
51. Kulik, H. J. Treating electron over-delocalization with the DFT+U method. *J. Chem. Phys.* **142**, 240901 (2015).
52. Kulik, H. J. & Marzari, N. Systematic study of first-row transition-metal diatomic molecules: a self-consistent DFT+U approach. *J. Chem. Phys.* **133**, 114103 (2010).

Acknowledgements

This work was financially supported by the National Natural Science Foundation of China (grant nos. T2325028 and 12274016) and the Ministry of Science and Technology (MOST) of China (grant nos. 2024YFA1409100 and 2024YFA1409201). L. Chen acknowledges support from the CAS

Project for Young Scientists in Basic Research (grant no. YSBR-054). Y.L. acknowledges the Zhejiang Provincial Natural Science Foundation of China (LRG25A040001 and LDT23F04014F01). Y.D. acknowledges the Beijing High Innovation Plan (grant no. 202504841020) and the Beijing Municipal Science and Technology Project (grant no. Z251100000725001). The authors acknowledge Quantum Scale Co., Ltd. for technical support in atomic force microscope experiments.

Author contributions

L. Chen proposed and conceived this project. D.T., J.D., S. Zhou and Z.L. contributed to the experiments under the supervision of L. Chen and Y.D. The theoretical model was provided by Y.L., and S. Zhong performed calculations under the supervision of Y.L. Help with data analysis was provided by K.C., W.Z., L. Cao, X.H., T.G., K.D., H.F., Y.W., K.W., P.C., S.W. and B.F. The manuscript was written by D.T., S. Zhong, Y.L. and L. Chen, with input and comments from all co-authors.

Competing interests

The authors declare no competing interests.

Additional information

Supplementary information The online version contains supplementary material available at https://doi.org/10.1038/s41563-026-02537-2.

Correspondence and requests for materials should be addressed to Yi Du, Yunhao Lu or Lan Chen.

Peer review information *Nature Materials* thanks the anonymous reviewers for their contribution to the peer review of this work.